

A dynamical perspective on atmospheric temperature variability and its response to climate change

Article

Published Version

Open Access

Tamarin-Brodsky, T., Hodges, K., Hoskins, B. J. and Shepherd, T. G. (2019) A dynamical perspective on atmospheric temperature variability and its response to climate change. *Journal of Climate*, 32 (6). pp. 1707-1724. ISSN 1520-0442 doi: <https://doi.org/10.1175/JCLI-D-18-0462.1> Available at <http://centaur.reading.ac.uk/81376/>

It is advisable to refer to the publisher's version if you intend to cite from the work. See [Guidance on citing](#).

To link to this article DOI: <http://dx.doi.org/10.1175/JCLI-D-18-0462.1>

Publisher: American Meteorological Society

All outputs in CentAUR are protected by Intellectual Property Rights law, including copyright law. Copyright and IPR is retained by the creators or other copyright holders. Terms and conditions for use of this material are defined in the [End User Agreement](#).

www.reading.ac.uk/centaur

CentAUR

Central Archive at the University of Reading

Reading's research outputs online

A Dynamical Perspective on Atmospheric Temperature Variability and Its Response to Climate Change

TALIA TAMARIN-BRODSKY

Department of Meteorology, University of Reading, Reading, United Kingdom

KEVIN HODGES

Department of Meteorology, and National Centre for Atmospheric Science, University of Reading, Reading, United Kingdom

BRIAN J. HOSKINS AND THEODORE G. SHEPHERD

Department of Meteorology, University of Reading, Reading, United Kingdom

(Manuscript received 19 July 2018, in final form 13 November 2018)

ABSTRACT


The atmospheric temperature distribution is typically described by its mean and variance, while higher-order moments, such as skewness, have received less attention. Skewness is a measure of the asymmetry between the positive and negative tails of the distribution, which has implications for extremes. It was recently shown that near-surface temperature in the Southern Hemisphere is positively skewed on the poleward side of the storm tracks and negatively skewed on the equatorward side. Here we take a dynamical approach to further study what controls the spatial structure of the near-surface temperature distribution in this region. We employ a tracking algorithm to study the formation, intensity, and movement of warm and cold temperature anomalies. We show that warm anomalies are generated on the equatorward side of the storm tracks and propagate poleward, while cold anomalies are generated on the poleward side and propagate equatorward. We further show that while the perturbation growth is mainly achieved through linear meridional advection, it is the nonlinear meridional advection that is responsible for the meridional movement of the temperature anomalies and therefore to the differential skewness. The projected poleward shift and increase of the temperature variance maximum in the Southern Hemisphere under global warming is shown to be composed of a poleward shift and increase in the maximum intensity of both warm and cold anomalies, and a decrease in their meridional displacements. An analytic expression is derived for the nonlinear meridional temperature tendency, which captures the spatial structure of the skewness and its projected changes.


1. Introduction

The temperature variability of Earth's atmosphere is often described using the first two moments of its probability density function (PDF), namely, the mean atmospheric temperature (Fig. 1a) and its variance

(Fig. 1b). The former naturally determines the mean climatology and its associated meridional temperature gradient, while the latter can involve short time scale changes, such as those due to passing cyclones and anticyclones. Temperature variance tends to maximize in midlatitudes, where atmospheric eddies are efficient in transferring heat poleward [e.g., in the Southern Hemisphere (SH) in Fig. 1b], and over the continents, where low thermal inertia results in large temperature contrasts with oceanic regions [e.g., in the Northern Hemisphere (NH) in Fig. 1b].

Both the mean climatological state and the temperature variance have been observed to change in recent years and are projected to continue changing in the future as a result of global warming (Bindoff et al. 2013). A large effort has been directed toward studying the mean

 Denotes content that is immediately available upon publication as open access.

 Supplemental information related to this paper is available at the Journals Online website: <https://doi.org/10.1175/JCLI-D-18-0462.s1>.

Corresponding author: Talia Tamarin-Brodsky, t.tamarin@reading.ac.uk

DOI: 10.1175/JCLI-D-18-0462.1

© 2019 American Meteorological Society. For information regarding reuse of this content and general copyright information, consult the [AMS Copyright Policy](https://www.ametsoc.org/PUBSReuseLicenses) (www.ametsoc.org/PUBSReuseLicenses).

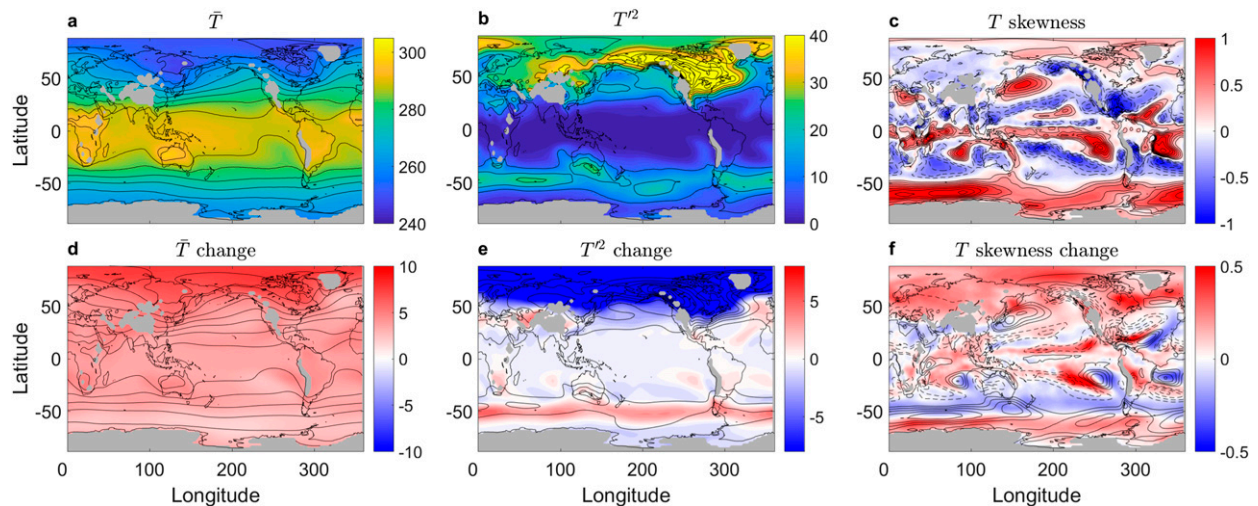


FIG. 1. The climatological 850-hPa (a) mean temperature (K), (b) temperature variance (K^2), and (c) temperature skewness based on ERA-Interim data, averaged over the years 1980–2014 during DJF. The corresponding projected changes (years 2080–99 minus 1980–99) in (d) mean temperature (K), (e) temperature variance (K^2), and (f) temperature skewness based on 26 CMIP5 RCP8.5 ensemble members. In (a)–(c), contours are added in addition to the color shading; in (a), the lowest contour equals 255 K and the contour interval equals 5.5 K; in (b), the lowest contour equals $10 K^2$ and the contour interval equals $7 K^2$; and in (c), the lowest contour equals ± 0.23 and the contour interval equals ± 0.16 . In (d)–(f), the same contours are used, respectively, to show the historical CMIP5 climatologies. Gray shading denotes regions where topography extends above the 850-hPa isobar.

atmospheric temperature response to climate change, as well as its variance and extremes (Schär et al. 2004; Fischer and Schär 2009; Volodin and Yurova 2013; Schneider et al. 2015, hereafter STH; Gao et al. 2015; Holmes et al. 2016). The multimodel mean response of climate change projections, such as from phase 5 of the Coupled Model Intercomparison Project (CMIP5) representative concentration pathway 8.5 (RCP8.5) high-emission scenario (Taylor et al. 2012), shows a mean temperature increase throughout the whole globe, with the largest increase occurring over the Arctic (Fig. 1d). This is often referred to as “Arctic amplification” (Manabe and Wetherald 1980; Screen and Simmonds 2010; Cohen et al. 2014) and is a consequence of the positive ice–albedo feedback (Arrhenius 1896), although other processes such as lapse rate feedback are also involved (Manabe and Wetherald 1975; Pithan and Mauritsen 2014).

In addition, multiple studies find a decrease of the temperature variance in the future in the NH during winter (Fig. 1e) on both interannual and synoptic time scales (de Vries et al. 2012; Screen 2014; Hassanzadeh et al. 2014; Screen et al. 2015; STH). A positive shift in the mean toward warmer temperatures and a decrease in variance generally implies a decrease in the frequency of extreme cold days with respect to a fixed threshold and an increase in warm days, as was indeed found by several authors (Easterling et al. 2000; Donat and Alexander 2012; Hansen et al. 2012; Rhines and Huybers 2013; Tingley and Huybers 2013; Coumou et al. 2013; Huntingford et al. 2013).

The skewness of the atmospheric temperature distribution has received less attention in the literature. It is formally defined as $S = \overline{T'^3} / (\overline{T'^2})^{3/2}$, where T' denotes the temperature anomalies, and bar signifies a time average. It measures the asymmetry between the positive and negative anomalies comprising the temperature distribution and is closely related to extreme temperature events as it mainly involves the tails of the distribution. However, it is currently still debated whether or not skewness is important for capturing the essence of the temperature variability. While several studies conclude that skewness is small and therefore not significant, at least on synoptic time scales (Swanson and Pierrehumbert 1997; Newman et al. 2010; STH), others point to its importance, especially when considering projected temperature changes (Petoukhov et al. 2008; Ruff and Neelin 2012; Loikith and Broccoli 2012; Huybers et al. 2014; Loikith et al. 2015; Garfinkel and Harnik 2017, hereafter GH; Linz et al. 2018).

For example, STH suggest that on synoptic time scales, near-surface temperature PDFs are essentially indistinguishable from a Gaussian. By using a Taylor expansion and assuming a linear approximation, STH were able to relate the temperature variance to the meridional background temperature gradient and an eddy mixing length scale. They showed in an ensemble of CMIP5 models that changes in near-surface temperature variance tend to follow changes in the meridional temperature gradient and concluded that to first order,

changes in the mean and variance are sufficient to account for changes even in extreme temperature events.

On the contrary, other studies point out that temperature PDFs are non-Gaussian (Petoukhov et al. 2008; Luxford and Woollings 2012; Perron and Sura 2013; Sardeshmukh et al. 2015). While bandpass filtering generally tends to make the PDFs more Gaussian (Proistosescu et al. 2016), some studies find deviations from Gaussianity even on synoptic time scales (GH). In addition, skewness was found to be important for climate change studies, since short-tailed distributions are much more sensitive to a change in the mean than long-tailed distributions (Ruff and Neelin 2012; Loikith and Broccoli 2012; Sardeshmukh et al. 2015; GH).

It has been shown that passive tracer dynamics with stochastic red noise (i.e., with a memory) can generate temperature skewness (Luxford and Woollings 2012; Perron and Sura 2013; Sardeshmukh et al. 2015). Recently, an attempt was made to relate skewness to dynamics (GH). By performing composites on extreme cold and warm temperature events in the SH lower troposphere, GH found that warm events are characterized by a cyclone (anticyclone) to the west (east), while the opposite is true for cold events. This contributes to the poleward advection of the warm temperature anomalies and the equatorward advection of the cold anomalies. GH also showed how the differential advection was achieved in a simple two-dimensional Lagrangian temperature advection model, initiated with an anticyclone–cyclone pair, when the nonlinear advection terms were retained. Consistent with these findings, Linz et al. (2018) showed how skewness can be generated in an idealized model where temperature is advected nonlinearly as a passive tracer by stochastically generated Rossby waves with a sustained background temperature gradient.

In this paper, we have extended both the previous studies of STH and GH. We investigate further the mechanisms leading to temperature skewness by taking a Lagrangian feature tracking approach and show explicitly the role of nonlinear meridional advection in generating it. The importance of considering the skewness in addition to variance when studying the temperature response to climate change is emphasized by the tracking. We also extend the linear approximation given in STH and show how the nonlinear term inevitably generates skewness.

We employ a tracking algorithm to identify and track temperature perturbations in reanalysis data, as well as in data from 26 CMIP5 models for the RCP8.5 scenario simulations (Taylor et al. 2012). We show the utility of the tracking approach in decomposing the temperature variance into warm and cold anomalies, as well as in recovering the spatial structure of the skewness. The temperature skewness becomes clearly apparent from

the tracking statistics and gives further insight into the propagation characteristics of the anomalies. We also perform composites on extreme warm and cold events, recovering the cyclone/anticyclone asymmetry found in GH, and investigate the temperature tendency equation to study which processes control the growth and movement of the temperature anomalies.

This study concentrates on the 850-hPa level (which is above the boundary layer), rather than on the surface temperature, to facilitate comparison with the previous studies of STH and GH, who both concentrated on the 850-hPa level. Studying the surface temperature is clearly important, as this is where the impacts of extremes are mostly felt. However, any dynamical arguments are immediately complicated by boundary layer processes such as drag, radiation, and soil–moisture interactions (Schär et al. 2004; Seneviratne et al. 2006; Fischer and Schär 2009). We therefore focus our attention on the near-surface temperature and note that our analysis is informative only about the dynamical origin of surface temperature anomalies. Nonetheless, we note that some correlation does exist locally between the 850-hPa temperature and the surface temperature during extreme warm and cold events in the SH (see Fig. S1 in the online supplemental material).

The paper is organized as follows. In section 2, a description of the data and methods is given. Section 3 investigates the Eulerian results for the temperature variance and skewness in reanalysis data, as well as the projected changes in the CMIP5 RCP8.5 models. In section 4, the tracking results are presented, including the temperature tendency composites, and the utility of the dynamical approach to decipher the Eulerian results is discussed. Finally, in section 5, we derive the analytic nonlinear expression that captures the structure of the skewness. Conclusions and summary are given in section 6.

2. Data and methods

a. Reanalysis data

We use the 6-hourly 850-hPa temperature field from the European Centre for Medium-Range Weather Forecasts (ECMWF) interim reanalysis dataset (ERA-Interim; Dee et al. 2011), covering a period of 35 years, from 1980 to 2014. We concentrate on the SH summer season (DJF), where the storm track is most zonally symmetric (Hoskins and Hodges 2005), but some results are also discussed for the SH winter season (JJA) in the conclusions. The background climatology is defined for every 6-hourly time period as its average over the 35 years in order to remove the influence of both the diurnal and the seasonal cycles on the temperature anomalies. Perturbations are then defined as deviations

from the 6-hourly seasonally varying climatology, with no further filtering applied.

b. CMIP5 data

We analyze the 6-hourly temperature data at 850 hPa from 26 models from the CMIP5 ensemble, forced by the RCP8.5 emissions scenario (Taylor et al. 2012; the full model list is given in the supplemental information). In all models, only the r11p1 ensemble member is used. The historical runs (1981–2000) include all the observed atmospheric forcings, including anthropogenic and natural sources, and in the projected runs (years 2080–99) the radiative forcing increases by about 8.5 W m^{-2} by year 2100. For each model, we calculate its own 6-hourly climatology in the historical and projected simulations separately, and perturbations are defined relative to the corresponding climatology. The linear trend in the mean climatologies (during the reference periods) as a result of global warming is not removed, but it was verified that it does not alter any of our conclusions or results. The CMIP5 data were obtained from the World Data Center for Climate (WDCC; available at <http://cera-www.dkrz.de/WDCC/ui/>).

c. Storm tracking algorithm

In this study, we use the spherical feature tracking algorithm TRACK (Hodges 1995, 1999). The procedure used to track temperature anomalies is slightly different from the more traditional cyclone tracking configuration. First, we do not spatially filter the large-scale background flow (with the typical 0–5 total spherical harmonic wavenumber filter). Instead, the background flow is defined as the 6-hourly climatology, which is removed prior to the tracking. The fields are then reduced to a T42 resolution to provide some smoothing, and the anomaly centers are identified as minima or maxima in the anomaly field. We track the 850-hPa temperature anomalies every 6h, and only features that live for more than 2 days are considered for the analysis. Positive and negative anomalies are tracked separately. However, we relax the criterion that features must be mobile (as is often applied for cyclones) in order to allow for more stationary perturbations (like heat waves) to be identified. We use a cutoff of 0.5 K for the identification of the temperature anomalies, but the results are relatively insensitive to this cutoff value. The genesis of features is defined as the first point of identification (unless this occurs at the first time step of the data), and the lysis of features is defined as the last point of the track (unless this occurs at the last time step of the data). Statistics for their spatial distribution are then generated using spherical kernel estimators (Hodges 1996).

d. Tracking composites of temperature tendency

The tracking results of 850-hPa warm and cold temperature anomalies are used to construct composites of the thermodynamic budget. The composites are constructed using only one CMIP5 model, ECHAM6 (MPI-ESM-LR), for which full data were obtained (since the standard CMIP5 output does not include all the needed fields). Only temperature anomalies that first appear between latitudes 30° and 70°S are used, to concentrate on the midlatitudes. In addition, composites are performed on the strongest 25th-percentile features, defined based on the maximum attained intensity of the tracked features (but similar results are obtained when all features identified are considered). The composites are constructed by placing a box of 30° latitude by 30° longitude around the center of each feature during the time of maximum intensity and then averaging together all other boxes. Overall, there are roughly 500 warm and 500 cold events constituting the composites.

3. Temperature variability and projected changes

Consistent with previous studies, the 850-hPa temperature skewness in ERA-Interim during DJF (Fig. 1c) exhibits rich latitudinal and longitudinal structure (Petoukhov et al. 2008; Perron and Sura 2013; Sardeshmukh et al. 2015; GH). Notable features include positive skewness over the Southern Ocean, in the tropics, and over the northern parts of the ocean basins in the NH. Negative skewness is obtained more in midlatitudes, mostly on the equatorward side of the midlatitude jet streams and storm tracks (around latitudes 30° – 40°S) and over Eurasia and western North America. There is an indication of a dipole structure in the skewness around regions where the temperature variance is maximized, especially in the SH (consistent with GH). Recall that positive skewness implies that the positive tail of the temperature PDF is longer than the negative tail (i.e., that strong positive anomalies are more frequent in regions of positive skewness, and similarly for negative skewness).

To determine whether these skewness values are significant, one can use the standard error for skewness, which is calculated as the variance of the skewness from a random sample of a normal distribution. An approximate expression to the standard error for skewness is given by $\sigma_S = \sqrt{(6/N_i)}$, where N_i is the number of independent degrees of freedom. Skewness values are then considered significant if they are larger in magnitude than $2\sigma_S$ (Holzer 1996). We estimate $N_i = 450$ (90 days for a season multiplied by the 35 years and divided by a typical atmospheric decorrelation time scale of 7 days). This gives $2\sigma_S \approx 0.23$, which is similar to

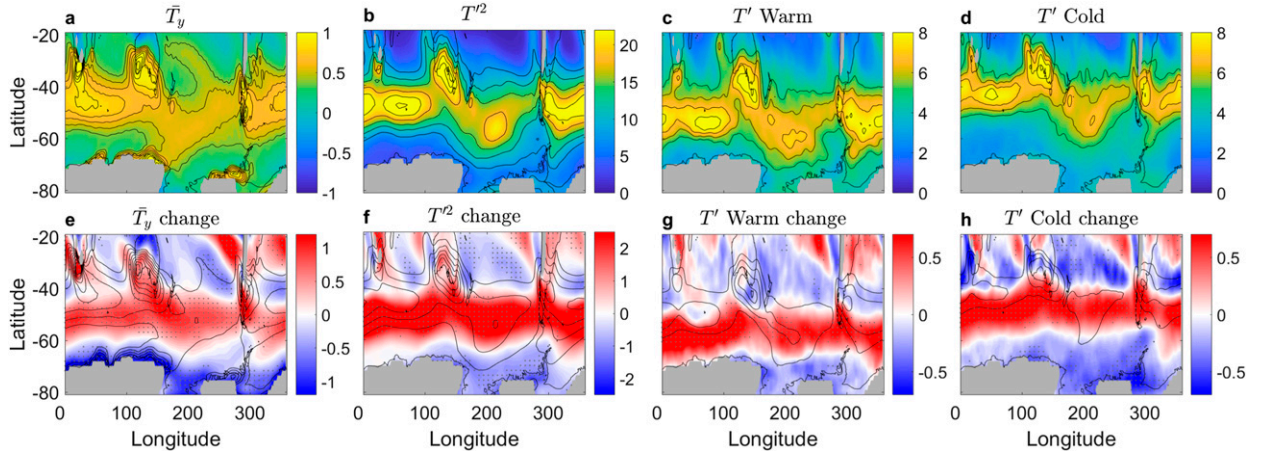


FIG. 2. The climatological 850-hPa SH (a) mean temperature gradient (10^{-5} K m^{-1}), (b) temperature variance (K^2), and mean intensity (absolute value, K) of (c) warm anomalies and (d) cold anomalies, produced from the tracking, and based on ERA-Interim data during DJF. The corresponding projected changes in (e) mean temperature gradient (10^{-5} K m^{-1}), (f) temperature variance (K^2), and mean intensity (absolute value, K) of (g) warm anomalies and (h) cold anomalies, based on 26 CMIP5 RCP8.5 ensemble members. In (a)–(d), contours are added in addition to the color shading. In (a), the lowest contour equals $0.4 \cdot 10^{-5} \text{ K m}^{-1}$ and the contour interval equals $0.1 \cdot 10^{-5} \text{ K m}^{-1}$; in (b), the lowest contour equals 10 K^2 and the contour interval equals 3 K^2 ; and in (c),(d), the lowest contour equals 5 K and the contour interval equals 1 K . In (e)–(h), the same contours are used, respectively, to show the historical CMIP5 climatologies. Gray shading denotes regions where topography extends above the 850-hPa isobar, and regions where more than 80% of the models agree on the sign of the change are stippled.

but a relatively stricter value compared to what was found in previous studies (Perron and Sura 2013). Skewness values larger than this threshold are highlighted in Fig. 1c using solid (for positive) or dashed (for negative) contours.

The ensemble mean projected change in skewness (Fig. 1f) shows mainly an increase in the NH and a poleward shift in the SH. Note that these projected changes are changes in skewness relative to the new climatological states. For example, the positive change in skewness in the NH occurs in addition to the shift toward warmer mean temperatures. For the rest of the paper, we concentrate on the SH during DJF, but some results for JJA are discussed in the conclusions. The NH will be investigated in a subsequent paper.

The observed meridional climatological temperature gradient in the SH maximizes in midlatitudes (Fig. 2a), and this is also the region where the temperature variance T'^2 is maximized (Fig. 2b). The collocation of the maxima of the mean meridional temperature gradient and the temperature variance is expected from the first-order linear approximation discussed in STH. Assuming small displacements of temperature anomalies and using a Taylor expansion, one can show that, to first order (STH),

$$T' \approx -\frac{\partial \bar{T}}{\partial y} \eta, \quad (1)$$

where $y = a\phi$, with a the radius of Earth, ϕ the latitude, and $\eta = y - y_0$ is the meridional displacement of the

temperature anomaly from its initial meridional location y_0 . In the SH, since $\partial \bar{T} / \partial y > 0$, a poleward air movement ($\eta < 0$) is consistent with a warm temperature anomaly, and an equatorward air movement ($\eta > 0$) is consistent with a cold temperature anomaly. Hence, the temperature variance scales, to first order, as

$$\overline{T'^2} \approx \left(\frac{\partial \bar{T}}{\partial y} \right)^2 \overline{\eta^2}, \quad (2)$$

where $\overline{\eta^2}$ can be regarded as the variance of the eddy mixing length scale (STH).

Relation (2) is probably a good approximation for the SH, where the lack of large land masses in midlatitudes results in a more zonally symmetric storm track. However, it fails, for example, to explain the temperature variance over the continents in the NH, where temperature gradients are actually low. Temperature variance over continents is potentially related to other processes such as localized zonal temperature gradients, soil-moisture feedbacks, or any other process not captured by the simple linear approximation (Schär et al. 2004; Seneviratne et al. 2006; Fischer and Schär 2009), but these are not the focus here.

The projected CMIP5 ensemble mean response in the SH shows mainly an intensification of the mean temperature gradient maximum in midlatitudes (Fig. 2e) and a slight poleward shift (the historical CMIP5 ensemble mean is shown in black contours for reference). There is also an apparent decrease of the temperature

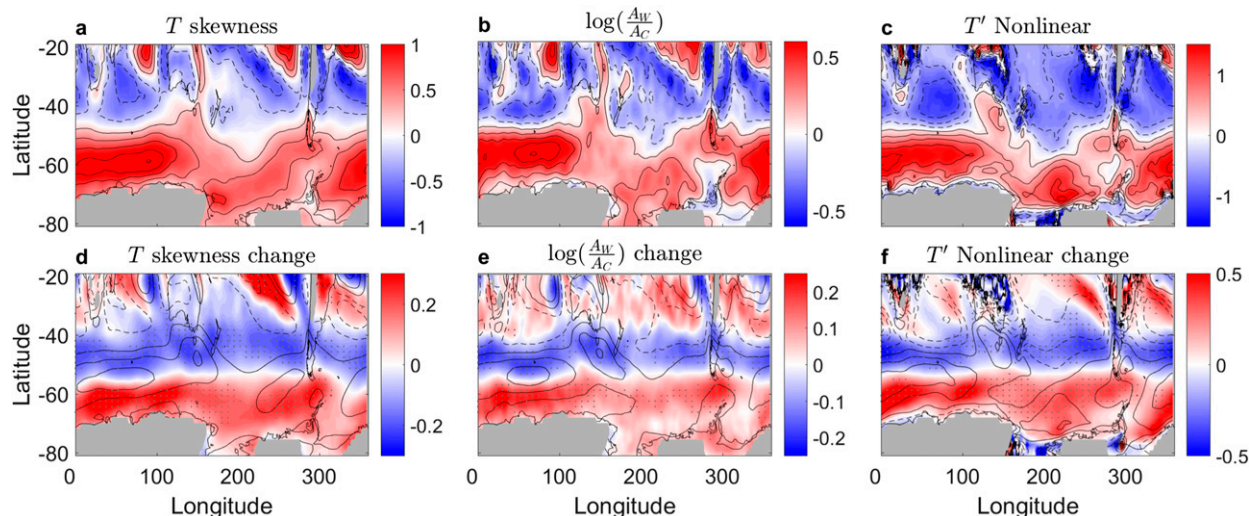


FIG. 3. The climatological 850-hPa SH (a) temperature skewness, (b) log of the ratio of mean intensity (absolute value) of warm anomalies to cold anomalies produced from the tracking, and (c) nonlinear approximation of the temperature perturbation due to nonlinear meridional advection (K), based on ERA-Interim data during DJF. The corresponding projected changes in (d) temperature skewness, (e) log of the ratio of warm anomalies to cold anomalies, and (f) nonlinear approximation, based on 26 CMIP5 RCP8.5 ensemble members. In (a)–(c), contours are added in addition to the color shading. In (a), the lowest contour equals ± 0.23 and the contour interval equals ± 0.3 ; in (b), the lowest contour equals ± 0.1 and the contour interval equals ± 0.2 ; and in (c), the lowest contour equals ± 0.2 and the contour interval equals ± 0.36 . In (d)–(f), the same contours are used, respectively, to show the historical CMIP5 climatologies. Gray shading denotes regions where topography extends above the 850-hPa isobar, and regions where more than 80% of the models agree on the sign of the change are stippled.

gradient poleward of 70°S , consistent with the findings of previous studies (e.g., Holmes et al. 2016). The intensification of the midlatitude temperature gradient is consistent with the projected warming patterns (i.e., with the enhanced surface warming in the tropical region; Fig. 1d in the SH). The change in temperature variance (Fig. 2f) seems to follow a similar pattern, with mostly an increase and a slight poleward shift of the variance maximum, accompanied by some decrease in the polar region.

While relation (2) can explain, to first order, the observed temperature variance and its projected changes through changes in the meridional temperature gradient (as discussed by STH), it does not capture the observed skewness structure (Fig. 3a). In fact, the linear approximation cannot, by construction, resolve the skewness, as this term is entirely symmetric for warm and cold anomalies. This important point will be discussed further in the next sections.

The temperature skewness in ERA-Interim is positively skewed poleward of 45°S and negatively skewed around the subtropical region, consistent with the results found by GH (see their Fig. 3). The projected CMIP5 change in temperature skewness (Fig. 3d) shows a very clear poleward shift in the midlatitudes, with a positive skewness change poleward of the historical maximum in skewness and a negative change equatorward of that. This is consistent with two previous idealized studies (GH; Linz et al.

2018), who found that a negative skewness change occurs in the midlatitudes (i.e., on the equatorward side of the jet) when the jet stirring latitude shifts poleward.

In the next section, we present the temperature tracking results and show how these can be used to reconstruct the Eulerian statistics, as well as to give further insights into their decomposition into warm and cold anomalies and the underlying processes.

4. Tracking temperature anomalies

a. Eulerian versus Lagrangian approaches

Using the 6-hourly 850-hPa temperature data from the reanalysis and the 26 CMIP5 ensemble members, the tracking algorithm is applied to track the temperature anomalies, as explained in section 2c. The tracking is performed separately for warm and cold anomalies, and statistics for their spatial distribution are then generated. For example, the spatial distribution of the mean intensity of features (Figs. 2c,d) shows clearly that warm and cold anomalies do not peak at the same latitudinal locations. While warm temperature anomalies tend to maximize on the poleward flank of T'^2 (Fig. 2c), cold anomalies are maximized on the equatorward flank (Fig. 2d). Their combined contribution (amplitudes squared; not shown) indeed results in a structure similar to the Eulerian temperature variance (Fig. 2b). However,

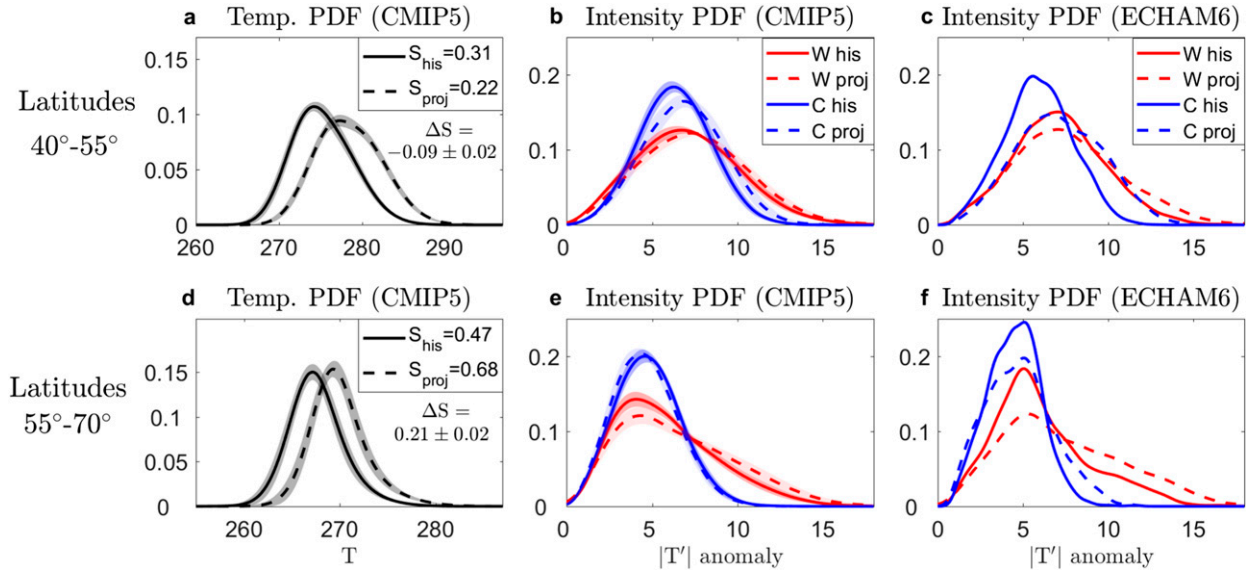


FIG. 4. The PDF of 850-hPa temperature (K) for the SH latitudinal band of (a) 40°–55°S and (d) 55°–70°S, and the PDF of 850-hPa intensity (absolute value) of warm (W; red) and cold (C; blue) temperature anomalies (K) from the tracking, for the SH latitudinal band of (b) 40°–55°S and (e) 55°–70°S, based on 26 CMIP5 RCP8.5 ensemble members in the historical (solid lines) and projected (dashed lines) during DJF. The PDFs are obtained using a kernel fitting, and the shading denotes the 95% confidence interval [calculated using a two-tailed t distribution with 26 degrees of freedom ($t_s \approx 2.06$) and multiplying by the standard error of the mean model spread for each temperature]. (c), (f) As in (b), (e), but for one model only, ECHAM6 (MPI-ESM-LR). In (a), (d), the skewness of the PDF (denoted as S_{his} and S_{proj} for the historical and projected simulations, respectively) is shown in the legend, including the mean projected skewness change and its uncertainty, estimated from the spread of the skewness change of individual models (see Fig. S3).

the tracking allows us to decompose directly the temperature variance into the different contributions of warm and cold anomalies, and therefore to reveal, for example, differences in location and strength.

Moreover, plotting the ratio of the warm to cold mean intensities (Fig. 3b; on a log scale, such that the ratio is of equal magnitude if either $A_w = 2A_c$ or $A_c = 2A_w$ where A_w and A_c are the mean intensities of warm and cold anomalies, respectively) recovers quite remarkably the structure of the skewness (Fig. 3a). This is perhaps not entirely surprising, given that the skewness is exactly the measure of the asymmetry between the warm and cold tails of the temperature distribution. Nonetheless, it gives further confidence in the tracking results and therefore in its utility in deciphering the observed structure and projected changes.

The projected increase and poleward shift of the SH temperature variance maximum (Fig. 2f) can now be decomposed into a shift and increase on the poleward side of T'^2 of warm anomalies (Fig. 2g) and a shift and increase on the equatorward side of T'^2 of cold anomalies (Fig. 2h). However, as we will see next, these changes are associated with different changes in the behavior of the warm and cold anomalies. Consistent with these changes, the projected change in the ratio of warm to cold anomalies shows a poleward shift relative

to the historical ratio (Fig. 3e), which is very similar to the projected change in the skewness (Fig. 3d).

The changes in variance and skewness described above can also be seen directly by comparing the PDFs of the 850-hPa temperature in different latitudinal bands (Figs. 4a,d). The Eulerian PDFs are calculated for all temperature anomalies from all models in a given latitudinal band (defined as deviations from the 6-hourly climatology), and the mean of each latitudinal band is then added. These are compared to the PDFs of intensity of anomalies from the tracking by isolating features that passed through each latitudinal band (Figs. 4b,e for the full CMIP5 ensemble and Figs. 4c,f for an example model, ECHAM6).

For example, the PDF of the latitudinal band between 40° and 55°S is positively skewed in the ensemble mean of the historical CMIP5 simulations (Fig. 4a; black line) and becomes less positively skewed in the projected simulations (Fig. 4a; dashed line). Consistent with that, the PDF of intensity of warm anomalies achieves its maximum at higher amplitudes than the cold anomalies in the historical simulations (Fig. 4b; solid red and red blue, respectively), which implies positive skewness. In the projected simulations, the cold anomalies intensify, while the warm anomalies only slightly intensify and remain almost unchanged (Fig. 4b; dashed red and blue

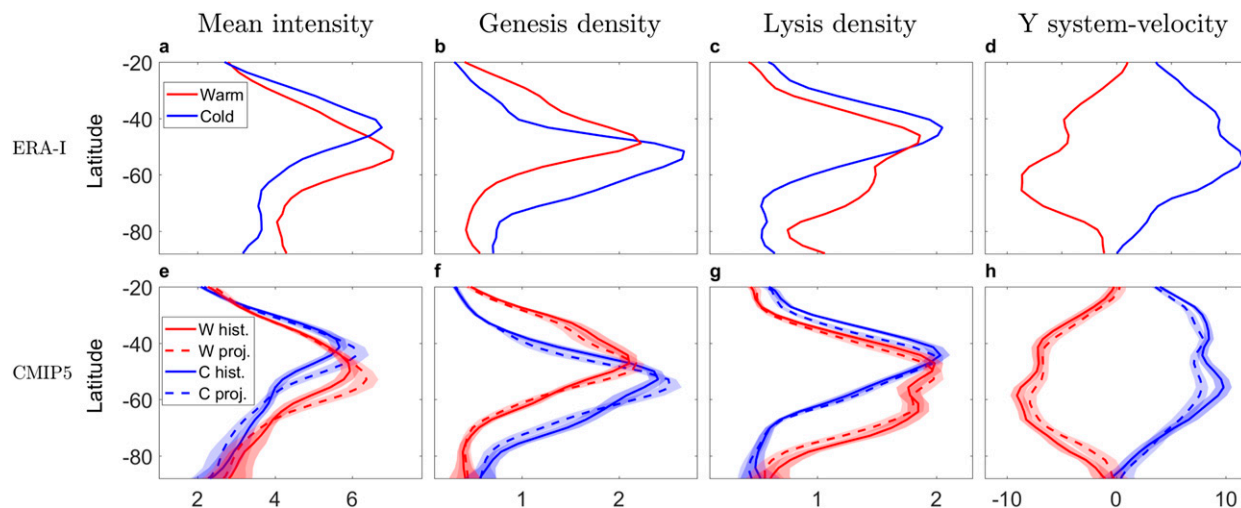


FIG. 5. Zonally averaged tracking statistics in the SH of 850-hPa (a) mean intensity (K), (b) genesis density, (c) lysis density, and (d) the meridional propagation velocity of systems (denoted as Y system velocity; m s^{-1}), for warm (red) and cold (blue) temperature anomalies produced from the tracking and based on ERA-Interim data during DJF. (e)–(h) The corresponding historical (solid lines) and projected (dashed lines) fields, based on 26 CMIP5 RCP8.5 ensemble members, for warm (W; red) and cold (C; blue) anomalies. The densities are given in number per unit area (a 5° spherical cap, $\sim 10^6 \text{ km}^2$) per month. The shading denotes the 95% confidence interval [calculated using a two-tailed t distribution with 26 degrees of freedom ($t_s \approx 2.06$) and multiplying by the standard error of the mean model spread for each latitude].

lines). Hence, variance increases, but the asymmetry decreases (warm anomalies are still stronger than cold anomalies, but less so). The signal is somewhat muted in the model ensemble average, since each model achieves its maximum and minimum skewness at slightly different latitudes, while the averaging is over fixed latitudes (Fig. S2). Therefore, we also show the same PDFs of mean intensities for one model only, ECHAM6 (MPI-ESM-LR), which shows more clearly the larger intensification of cold anomalies compared to warm anomalies in this latitudinal band (Fig. 4c).

In the latitudinal band between 55° and 70°S , the positively skewed PDF becomes even more positively skewed (Fig. 4d). Consistent with this, in the historical simulations, the warm anomalies are stronger, and they intensify even more in the projected simulations (Fig. 4e), so both variance and skewness increase. A similar trend is observed in ECHAM6 (Fig. 4f), where both anomalies intensify, but the warm anomalies intensify more such that overall the positive skewness increases. A statistical significance assessment of the skewness changes and model spread for the two latitudinal bands is shown in Fig. S3.

Note that the Eulerian projected change in the skewness alone (i.e., if it becomes more negative or more positive in a region) is not enough to determine the overall response. For example, if there is a negative change in skewness, one cannot determine from this alone whether it is the cold anomalies that intensify or the warm anomalies that weaken. The answer depends

also on the change in variance; if skewness changes negatively and variance increases, it must be that cold anomalies intensify (and if variance decreases, it implies that warm anomalies weaken). This statement is also true for variance changes alone; for example, if variance increases, this information alone is not enough to determine whether the increase is due to an increase in the magnitude of cold or warm anomalies (or both). This is obviously a crucial point that can have significant implications for the local weather and climate, and it points to the importance of studying temperature skewness in addition to temperature variance. The Lagrangian tracking approach is useful as it immediately gives the complete information about the intensities of warm and cold anomalies and their projected changes.

b. Statistics of tracking temperature anomalies

The tracking results give further insight into the different nature of the warm and cold anomalies, such as their formation, dissipation, intensity, and movement. Figure 5 shows the zonally averaged tracking statistics for the mean intensity (Figs. 5a,e), genesis (Figs. 5b,f), lysis (Figs. 5c,g), and meridional velocity (Figs. 5d,h), both in reanalysis data (Figs. 5a–d) and in the CMIP5 ensemble mean historical and projected simulations (Figs. 5e–h; solid and dashed lines, respectively). The genesis and lysis describe where the systems are generated or terminated, respectively, and are analogous to cyclogenesis and cyclolysis, which are often used in the cyclone-tracking literature. Their exact definition for

the calculation performed is given in the methods section.

The tracking statistics clearly show that warm anomalies are more intense on the poleward flank of the midlatitude storm track, whereas cold anomalies are strongest more equatorward (red and blue lines in Fig. 5a, respectively). Consistent with intuition, cold anomalies are generated closer to the pole, while warm anomalies are generated more equatorward (Fig. 5b). Correspondingly, warm anomalies dissipate poleward of where they are generated, while the lysis of cold anomalies occurs closer to the equator (Fig. 5c). This is consistent with the observed negative meridional system velocity of warm temperature anomalies and the positive meridional system velocity of cold anomalies (Fig. 5d).

The historical mean CMIP5 results generally agree with the reanalysis data (Figs. 5e–h; blue and red solid lines). The zonally averaged response in the projected simulations (Figs. 5e–h; dashed blue and red lines) shows mainly an increase in the intensity of both warm and cold anomalies in midlatitudes (Fig. 5e), with some decrease in both intensities at higher latitudes. The zonally averaged intensities and their projected changes capture the skewness and variance structure changes discussed earlier.

The genesis of both warm and cold anomalies shifts slightly poleward and also decreases at higher latitudes (mainly for the cold anomalies), so genesis becomes more concentrated in midlatitudes (Fig. 5f). These changes are consistent with the observed meridional temperature gradient changes (Fig. 2e). The poleward shift of the mean meridional temperature gradient maximum, which is potentially related to the poleward expansion of the Hadley cell (Yin 2005), implies that it is more difficult to generate both warm and cold anomalies in the subtropical regions, where temperature is more uniform. In addition, the decrease in the temperature gradient in the polar regions (Fig. 2e) implies that it is harder to generate anomalies there. On the other hand, the increase of the temperature gradient in the midlatitudes (Fig. 2e) makes it easier to generate both warm and cold anomalies in this region.

Interestingly, the lysis of both warm and cold anomalies also becomes more concentrated in midlatitudes (Fig. 5g). The lysis of warm anomalies occurs less at high latitudes, while the lysis of cold anomalies occurs less at low latitudes, and a consistent response is also seen by the decrease of the averaged meridional system velocities (Fig. 5h). The decrease in the meridional system velocities corresponds to a decrease in the meridional displacements of temperature anomalies.

At first glance, the decrease in the meridional displacements of temperature anomalies might seem consistent

with the argument that a stronger zonal flow [which is indeed found for the SH CMIP5 ensemble mean; e.g., Barnes and Polvani (2013); see also Fig. S4] corresponds to less meridional dispersion or a less “wavy” jet, just as a weaker zonal flow has been argued in the case of Arctic amplification to lead to a more wavy jet (Francis and Vavrus 2012). However, such an argument ignores the fact that the relative phase speed of the waves might change as well. Indeed, both the zonal mean low-level westerly jet and the eastward propagation of the low-level temperature anomalies strengthen in the projected climate simulations of CMIP5 (note that the low-level temperature anomalies are propagating eastward relative to the low-level jet, like surface Eady edge waves). The zonal flow increases more, such that the relative speed between the temperature anomalies and the jet decreases (see Fig. S4). This would suggest, through Eq. (15) of Bretherton (1966), that meridional displacements should actually increase. One must recall, however, that such an argument ignores the other variables that appear in the equation, such as the amplitude of the anomaly and its wavenumber and growth rate.

Note that from the linear approximation (2), one finds $\overline{\eta^2} = \overline{T'^2} (\partial \overline{T} / \partial y)^{-2}$; hence, it is clear that changes in the meridional displacements of temperature anomalies are related to changes in both the temperature variance and the meridional background temperature gradient. In the projected CMIP5 change in the SH, both the temperature variance and the meridional background temperature gradient maximum increase (and shift poleward). It turns out the relative increase of the meridional temperature gradient in the midlatitudes is larger than that of the temperature variance, consistent with $\overline{\eta^2}$ decreasing there (see Fig. S5). Note that while this gives a consistent picture between the Eulerian and Lagrangian views, it does not explain the observed changes (i.e., it still remains unclear why relative changes in the gradient are stronger than relative changes in the variance).

c. Temperature tendency composites for extreme events

Next, we investigate the thermodynamic budget for extreme warm and cold anomalies to study what controls their propagation and growth. Extreme events are defined as the strongest 25th percentile of each sign, determined from the PDFs of maximum intensity from the tracking (as in Figs. 4d–f, but for features in the latitudinal band between 30° and 70°S). The threshold values obtained are 10.5 and 9.5 K for the warm and cold anomalies, respectively. The composites are performed only for one CMIP5 model, ECHAM6 (MPI-ESM-LR), since full 6-hourly data are required for the

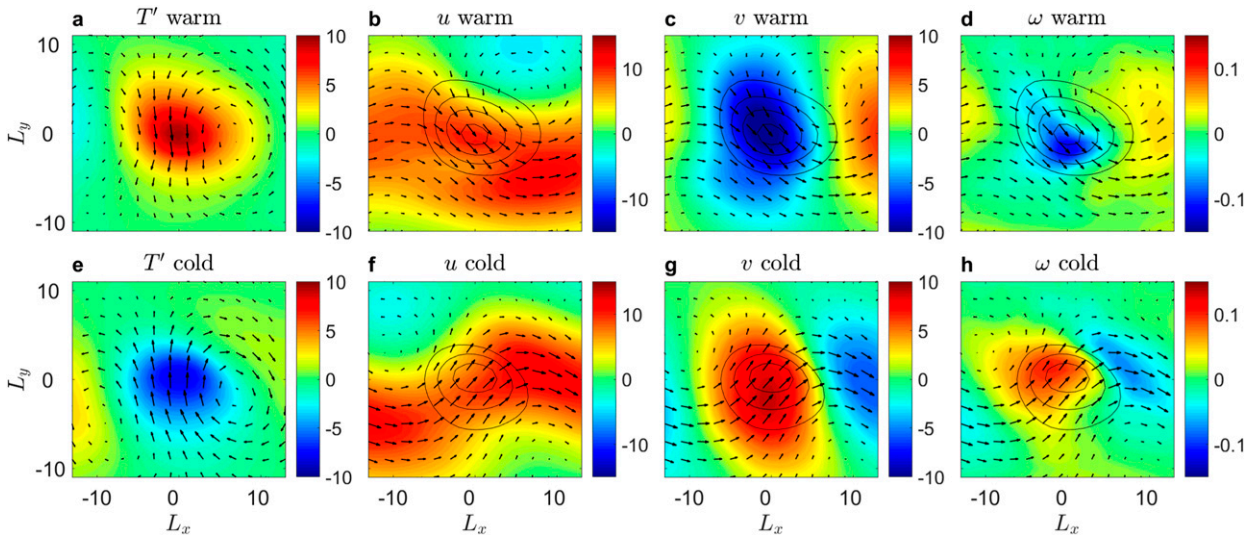


FIG. 6. Composites of 850-hPa (a) temperature anomaly (K), (b) zonal velocity ($\text{m}\cdot\text{s}^{-1}$), (c) meridional velocity ($\text{m}\cdot\text{s}^{-1}$), and (d) vertical velocity in pressure coordinates $\omega = dp/dt$ ($\text{Pa}\cdot\text{s}^{-1}$), produced by tracking the positive 850-hPa temperature anomalies in an example CMIP5 model, ECHAM6 (MPI-ESM-LR), in the historical simulation. Black arrows in (a) denote the anomalous composite velocity field and in (b)–(d) the full velocity. (e)–(h) The same composites, but for the cold temperature anomalies. The black contours in (b)–(d) and (f)–(h) show the corresponding low-level (850 hPa) temperature anomaly (where the lowest contour equals 2 K, and contour intervals equal 2 K); L_x and L_y denote the longitudinal and latitudinal distance (in $^\circ$), respectively, from the center of the composite box.

temperature tendency budget (and CMIP5 currently output only limited data on pressure levels). Note that similar results are obtained for the reanalysis data (not shown).

The composites of warm and cold temperature anomalies and the associated anomalous velocity field (Figs. 6a,e) clearly show that warm anomalies are located exactly between an anomalous anticyclonic circulation to the east and an anomalous cyclonic circulation to the west, while cold anomalies are located exactly between an anomalous cyclonic circulation to the east and an anomalous anticyclonic circulation to the west, as shown by GH. The composite of warm anomalies has a larger magnitude, since overall the temperature perturbations are positively skewed in the SH midlatitudes (e.g., Figs. 3a, 5a).

The composites of the full zonal flow (Figs. 6b,f) and meridional flow (Figs. 6c,g) show that the warm and cold anomalies are located in different phases of the wavy jet (black contours denote the corresponding temperature anomaly, and arrows show the full composite velocity). The warm anomalies are located to the east of the low-level wave trough (Fig. 6b) (recall this is the SH, so the low-level trough is associated with anomalous clockwise circulation) and are therefore in phase with the negative meridional velocity (Fig. 6e), while cold anomalies are located to the east of the low-level wave ridge (Fig. 6e) and are therefore collocated with the positive meridional velocity (Fig. 6f). In addition, warm anomalies are generally associated with upward vertical velocity (negative pressure velocity, $\omega = dp/dt$; Fig. 6d) and cold

anomalies with downward vertical velocity (Fig. 6h), as expected.

We next investigate the different contributions to the temperature tendency equation, given by

$$\frac{dT}{dt} = \frac{\alpha}{C_p} \omega + Q_T + R_T, \quad (3)$$

where $d/dt = (\partial/\partial t) + (u\partial/\partial x) + (v\partial/\partial y) + (\omega\partial/\partial p)$ is the material derivative, T is the temperature, $\alpha = 1/\rho$ where ρ is density, and $\partial/\partial x = \partial/(a \cos\phi\partial\lambda)$, $\partial/\partial y = \partial/a\partial\phi$, where λ and ϕ are the zonal and meridional coordinates, respectively. The RHS includes the adiabatic expansion term $(\alpha/C_p)\omega$, the diabatic heating due to latent heat release Q_T , which is calculated using the expression given by Emanuel et al. (1987), and all other forcing is denoted as R_T and calculated as a residual. The residual can include nonconservative forcing such as friction, radiation, and heat fluxes from the boundary layer.

Decomposing the total flow into a mean and a perturbation (i.e., $a = \bar{a} + a'$), where a is some field, the bar denotes the mean, and the prime denotes the perturbation, one finds

$$\begin{aligned} \frac{\partial T'}{\partial t} = & -\bar{u} \frac{\partial T'}{\partial x} - \bar{v} \frac{\partial \bar{T}}{\partial y} - \bar{u}' \frac{\partial T'}{\partial x} - \bar{v}' \frac{\partial T'}{\partial y} + \frac{\alpha}{C_p} \omega' \\ & - \omega' \frac{\partial \bar{T}}{\partial p} + Q'_T + R'_T, \end{aligned} \quad (4)$$

where we have neglected terms that involve $\partial \bar{T}/\partial x$, \bar{v} , $\bar{\omega}$, $\partial T'/\partial p$, and the mean flux terms $-\bar{u}'(\partial T'/\partial x)$ and

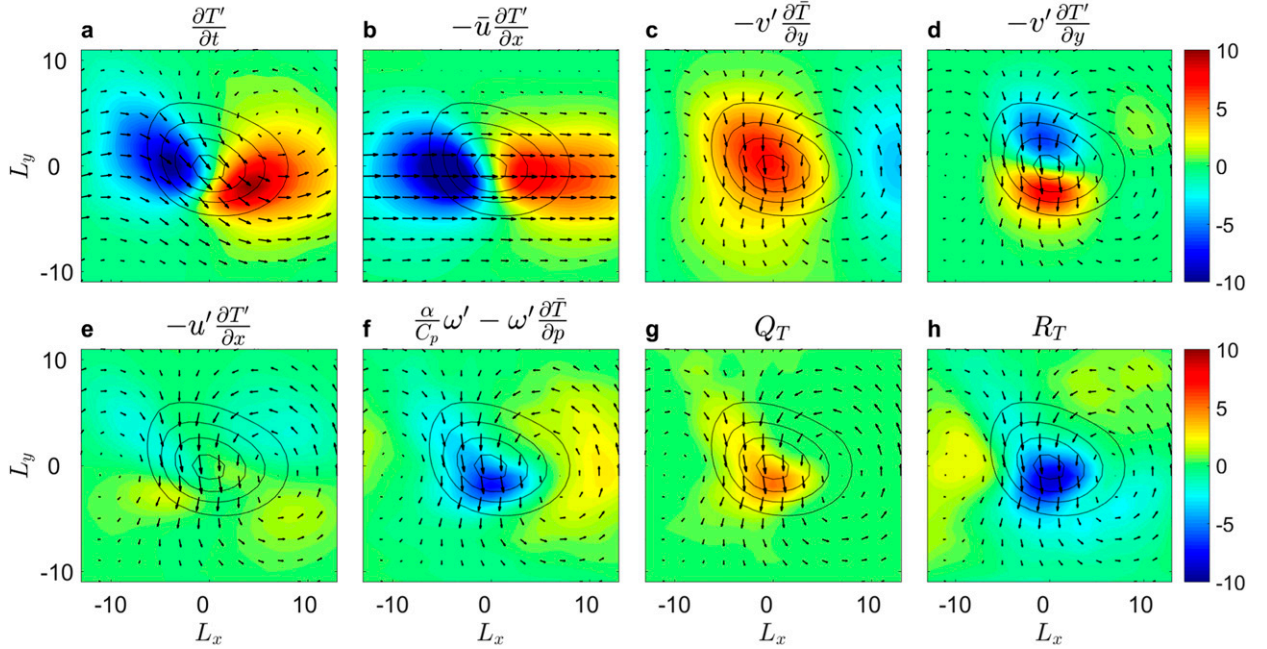


FIG. 7. Composites of temperature tendency (in units of 10^{-5} K s^{-1}) at 850 hPa following warm anomalies: (a) instantaneous temperature tendency $\partial T'/\partial t$ and a decomposition of this term into temperature tendency due to (b) zonal mean flow advection $-\bar{u}(\partial T'/\partial x)$, (c) linear meridional advection of mean temperature $-v'(\partial \bar{T}/\partial y)$, (d) nonlinear meridional advection of temperature perturbation $-v'(\partial T'/\partial y)$, (e) nonlinear zonal advection of temperature perturbation $-u'(\partial T'/\partial x)$, (f) vertical advection and adiabatic expansion $-(g/C_p)\omega' - \omega'(\partial \bar{T}/\partial p)$, (g) diabatic processes associated with latent heat release Q_T , and (h) temperature tendency due to residual forcing R_T . The composites are produced by tracking the positive 850-hPa temperature anomalies in an example CMIP5 model, ECHAM6 (MPI-ESM-LR), in the historical simulation. The black contours show the low-level (850 hPa) temperature anomaly (where the lowest contour equals 2 K, and contour intervals equal 2 K). The arrows in (a) show the total velocity field, in (b) the mean velocity field, and in (c)–(h) the anomalous velocity field in the composite; L_x and L_y denote the longitudinal and latitudinal distance (in $^\circ$), respectively, from the center of the composite box.

$-v'(\partial \bar{T}/\partial y)$, since they are found to be an order of magnitude smaller. Note that here, the climatological flow is also time dependent since we defined it as the 6-hourly climatology; however, its time derivative (which is an order of magnitude smaller) cancels out with the other mean products not included in Eq. (4).

The composite of each of these terms is shown in Figs. 7 and 8 for warm and cold anomalies for the historical simulation, respectively. The overall instantaneous temperature tendency of warm anomalies is eastward and poleward (Fig. 7a), while it is eastward and equatorward for cold anomalies (Fig. 8a). The eastward component of these tendencies originates from the zonal mean flow advection term in both cases (Figs. 7b, 8b).

The anomalous negative meridional velocity associated with warm extremes contributes to their growth through the advection of background warm air from lower latitudes ($-v'\partial \bar{T}/\partial y$; Fig. 7c) and similarly for cold anomalies through positive meridional velocity, which advects cold air from higher latitudes (Fig. 8c). This term, which involves the linear meridional advection of the background temperature by the anomalous wind, is

exactly the linear approximation used by *STH* and given in Eq. (1). This is similar to the linear term that describes baroclinic growth in the Eady model, where the surface temperature anomaly can be thought of as taking the form of a surface potential vorticity (PV) anomaly. Note, however, that this term can only contribute to the growth of the anomaly (and therefore to the variance), but not to its skewness since it is single signed and symmetric equatorward and poleward of the anomaly maximum.

On the contrary, the nonlinear meridional advection term $-v'\partial T'/\partial y$, which involves the anomalous advection of the anomalous temperature, produces an asymmetric tendency dipole and involves the poleward advection of the warm temperature anomalies and equatorward advection of the cold anomalies (Figs. 7d, 8d for warm and cold, respectively). This is the term that mostly contributes to the poleward (equatorward) motion of the warm (cold) anomalies and therefore to the differential skewness. In both cases, it contributes to a positive temperature tendency on the poleward side of the anomalies and to a negative tendency on the

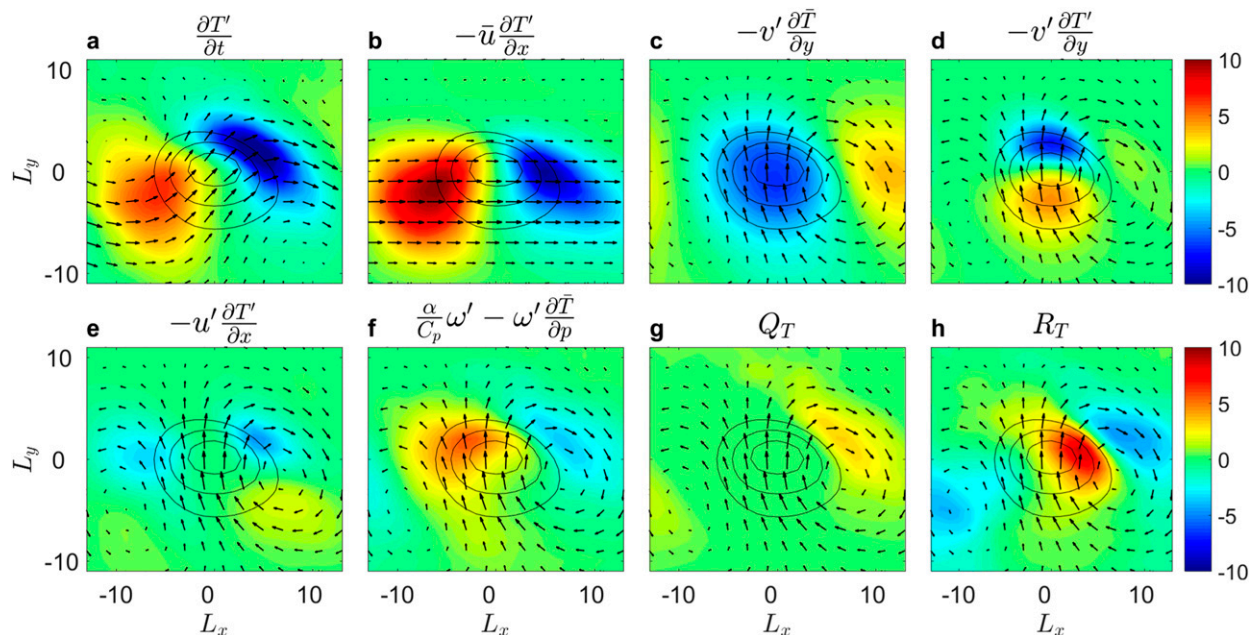


FIG. 8. As in Fig. 7, but for the cold anomalies.

equatorward side (Figs. 7d, 8d). This will inevitably contribute to differential advection and skewness

An important point to note is that even for a neutral surface temperature anomaly in isolation or for temperature advected as a passive tracer (as in Linz et al. 2018), skewness can still be generated if the nonlinear advection is taken into account. This is because for any perturbation T' generated linearly by $-v' \partial \bar{T} / \partial y$, the correlations between v' and T' are such that they are in antiphase (or in phase in the NH). Hence, nonlinear advection leading to differential skewness is also taking place.

For completeness, we also analyze the rest of the temperature tendency budget. For both warm and cold extremes, the zonal nonlinear advection term $-u' \partial T' / \partial x$ contributes essentially nothing or very little to the temperature tendency (Figs. 7e, 8e) since the anomalous zonal velocity field is approximately $\pi/2$ out of phase with the temperature anomaly, as discussed earlier. The vertical term, which includes both vertical advection $-\omega' \partial \bar{T} / \partial p$ and the adiabatic expansion term $\alpha / C_p \omega'$, contributes mostly negatively (positively) to the warm (cold) anomalies (Figs. 7f, 8f for warm and cold, respectively).

For the warm anomalies, which are associated with upward vertical motion (Fig. 6d), the vertical term roughly balances the warming due to latent heating Q_T , which contributes positively to the temperature where the air ascends and the water vapor condenses (Fig. 7g). Note that the latent heating maximizes at

higher altitudes, around 500–600 hPa (not shown), which is why such a small signal is observed at 850 hPa. This cancellation is absent for the cold anomalies, which are characterized mainly by downward vertical velocity (Fig. 6h), although some latent heat release occurs on the cyclonic side to the east of the cold extremes (Fig. 8g).

Finally, the residual term R_T , which can include friction, radiation, and heat fluxes from the boundary layer, is mainly negative for the warm extremes and positive for the cold extremes (Figs. 7h, 8h for warm and cold anomalies, respectively). It mainly acts to damp the temperature anomalies and to oppose the poleward (equatorward) tendency of warm (cold) anomalies. This is probably dominated by sensible heat flux from the underlying ocean, which becomes much colder as the warm anomalies propagate poleward into the high latitudes, and vice versa for the cold anomalies.

Note that other processes not considered here, such as soil–moisture interaction [which are known to affect, for example, heat waves over continental regions; e.g., Fischer and Schär (2009)], may be important for the growth and movement of temperature anomalies over land. However, these are not the focus of the current study, which aims to emphasize the role of nonlinear meridional advection in generating temperature skewness, and is concentrated on the SH where most of the data are over the ocean.

In the projected composites (not shown), the most notable change is a decrease in the meridional anomalous

Linear vs. nonlinear temperature advection (SH)

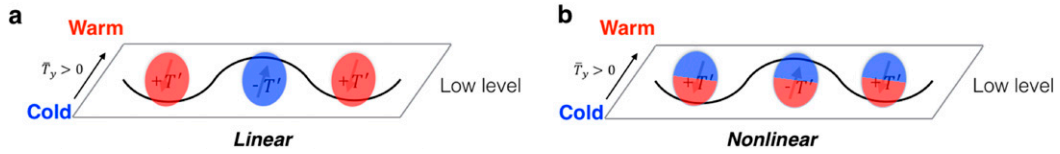


FIG. 9. A schematic illustration of the (a) linear vs (b) nonlinear meridional temperature advection in the SH. (a) The sign of the linear temperature tendency depends on the sign of the displacement (or v'), and is single-signed poleward and equatorward of where T'^2 is maximized. In contrast, in (b), the sign of the nonlinear temperature tendency does not depend on the sign of the displacement (or v') and is always positive poleward and negative equatorward of where T'^2 is maximized.

velocities, consistent with the decrease in the meridional propagation velocities found earlier (Fig. 5h). There is also no significant change in the temperature tendency due to latent heating, which indeed intensifies in the warmer climate, but mainly at the midlevels of the troposphere.

5. Nonlinear approximation

We now examine an extension of the linear approximation made by *STH* to include the main essence of the nonlinear meridional advection that leads to the differential temperature tendencies and thereby to the skewness.

We consider a heuristic model where the horizontal temperature field is a passive tracer with a constant time-independent meridional background temperature gradient. Motivated by the composites shown in Fig. 6, our main assumption is that v' is in antiphase with T' , while u' is $\pm\pi/2$ out of phase with T' (Fig. 6a).

We assume that the background flow is at rest, and the background temperature is zonally symmetric, such that $\partial\bar{T}/\partial x = 0$ but $\partial\bar{T}/\partial y > 0$ (as in the SH). We then investigate the horizontal temperature advection, given by

$$\frac{\partial T}{\partial t} + u \frac{\partial T}{\partial x} + v \frac{\partial T}{\partial y} = 0. \quad (5)$$

Dividing into a background quantity and a perturbation (i.e., $T = \bar{T} + T'$, $v = v'$, and $u = u'$), and linearizing Eq. (5), one can easily recover the linear approximation given earlier in Eq. (1) and discussed in *STH*:

$$T'_L \approx -\eta \frac{\partial \bar{T}}{\partial y}, \quad (6)$$

where $\partial\eta/\partial t = v'$ defines the meridional parcel displacement.

We next seek the second-order solution of Eq. (5) and use the linear approximation to estimate the nonlinear

tendency. The derivation is given in the [appendix](#), where it is shown that

$$T'_{NL} \approx \frac{1}{2} \frac{\partial \bar{T}}{\partial y} \frac{\partial(\eta^2)}{\partial y} \quad (7)$$

is an approximation to the temperature perturbation due to nonlinear advection.

An alternative expression can be obtained by replacing η^2 with its linear approximation using $T'^2 = \eta^2(\partial\bar{T}/\partial y)^2$, which gives

$$T'_{NL} \approx \frac{1}{2} \left(\frac{\partial \bar{T}}{\partial y} \right)^{-1} \frac{\partial(T'^2)}{\partial y}. \quad (8)$$

Now, it can be readily understood by either of the nonlinear expressions (7) or (8) why skewness changes sign around the maximum of η^2 or T'^2 and why zero skewness is achieved for the linear expression (6). Assuming $\partial\bar{T}/\partial y > 0$ is positive (e.g., in the SH temperature decreases from the equator to the pole) and constant, poleward displacements ($\eta < 0$) generate a positive linear temperature anomaly $T'_L = -\eta(\partial\bar{T}/\partial y) > 0$, while equatorward ($\eta > 0$) displacements generate a negative linear temperature anomaly $T'_L = -\eta(\partial\bar{T}/\partial y) < 0$ (Fig. 9a). Since air parcels that generate temperature anomalies are advected by propagating cyclones and anticyclones (hence a propagating wavy structure), and these waves propagate mainly in the midlatitude storm track region, in the time average the positive and negative anomalies cancel out on either side of the storm track, and hence zero skewness is achieved (i.e., there is no preferential sign for temperature anomalies on either side of the storm track).

In contrast, the nonlinear expression always gives a positive tendency poleward of the displacements and a negative tendency equatorward of the displacements, regardless of whether $\eta > 0$ or $\eta < 0$. This is because $\partial(\eta^2)/\partial y$ (or similarly $\partial(T'^2)/\partial y$) is always positive poleward of where the displacement is maximized and

negative equatorward of the maximum, so $(\partial\bar{T}/\partial y)$ $[\partial(\eta^2)/\partial y]$ always gives a dipole (Fig. 9b). This is exactly what was found in the composites of the meridional nonlinear advection terms for warm and cold anomalies presented in Fig. 7d and Fig. 8d, respectively, which both give the same signed dipole. It can then be understood how in the time mean, these temperature tendencies do not cancel out, and the picture obtained is a positive skewness on the poleward side of where η^2 or T'^2 is maximized (i.e., in the midlatitude storm track) and a negative skewness on the equatorward side.

The nonlinear expression (8) can also be evaluated in an Eulerian time mean sense by replacing $\partial(\bar{T}^2)/\partial y$ with $\partial(T'^2)/\partial y$, which can then be compared to the observed structure of the temperature skewness. The evaluated nonlinear expression for the reanalysis data in the SH (Fig. 3c) captures nicely the dipole skewness structure and compares well with the observed skewness (Fig. 3a). Moreover, the projected CMIP5 change of the nonlinear term (Fig. 3f) captures correctly the poleward shift and overall structure of the projected skewness change (Fig. 3d).

In a recent paper, Linz et al. (2018) argued, based on numerical simulations with an advection–diffusion model, that temperature skewness depends on eddy mixing properties rather than on the temperature gradient (they found that skewness remained fixed even when the background temperature was varied). Their numerical result can be understood from expressions (6) and (7) here. Since both T'_L and T'_{NL} are linearly proportional to \bar{T}_y (and hence also $T' \approx T'_L + T'_{NL}$), the skewness $S = T'^3/(T'^2)^{3/2}$ is independent of \bar{T}_y when the eddy mixing properties are fixed [as was the case in Linz et al. (2018), where temperature was stirred externally by stochastically generated Rossby waves]. However, in practice, the eddy displacements respond to changes in the temperature gradient as well. Hence, as a result of these changes to the eddy displacements, the skewness can be expected to change when the temperature gradient changes.

Our derived approximation of the nonlinear meridional advection term perhaps applies more to the SH, where our assumptions are more justified. In the NH, the presence of zonal temperature gradients complicates the situation, and other processes also take place. However, expression (8) essentially implies that to first order, changes in skewness would tend to follow changes in both the meridional temperature gradient and the temperature variance. In the SH, this is manifested mainly as a poleward shift, but in the NH, both these quantities might change in a more complicated manner.

6. Summary and discussion

In this study, we have investigated the atmospheric temperature variability and its projected changes from a

dynamical perspective. We applied a tracking algorithm to identify temperature anomalies and follow their centers in reanalysis data and in an ensemble of CMIP5 models, concentrating on the SH because of its simpler dynamical setting.

The separate tracking of warm and cold anomalies allows the decomposition of the Eulerian temperature variance, which does not distinguish between positive and negative anomalies, into their distinct contributions and thus to recover also the structure of the skewness. This approach is similar to the more common Lagrangian tracking approach used to study midlatitude storm tracks in order to separate the cyclones and anticyclones that compose it, which provides complementary information to the traditional Eulerian perspective (Hoskins and Hodges 2002).

The main results and conclusions from the current study can be summarized as follows:

- 1) Warm anomalies are generated on the equatorward side of the midlatitude storm track, propagate poleward, and reach their maximum intensity on the poleward side of the storm track. In contrast, cold anomalies are generated on the poleward side of the midlatitude storm track, propagate equatorward, and reach their maximum intensity on the equatorward side of the storm track. This is consistent with the positive skewness of the temperature variability found in high latitudes and the negative skewness found in low latitudes.
- 2) The current study emphasizes the importance of skewness and its crucial role for deciphering future changes. Both temperature variance and skewness are important when considering the projected temperature variability changes under global warming. For example, some regions with increased temperature variance exhibit an increase in the intensity of warm anomalies, while other regions exhibit an increase in the intensity of cold anomalies (relative to the new warmer mean). This can obviously have crucial implications for local weather and climate in different regions, and it points to the importance of studying the skewness in addition to variance changes. It also highlights the utility of the Lagrangian tracking approach, where the response can be seen directly by investigating the PDFs of intensity of warm and cold anomalies.
- 3) In the SH during DJF, both the temperature variance maximum and the meridional background temperature gradient maximum increase and slightly shift poleward. In addition, both the genesis and lysis of warm and cold anomalies become more confined to the midlatitudes, the former being consistent with

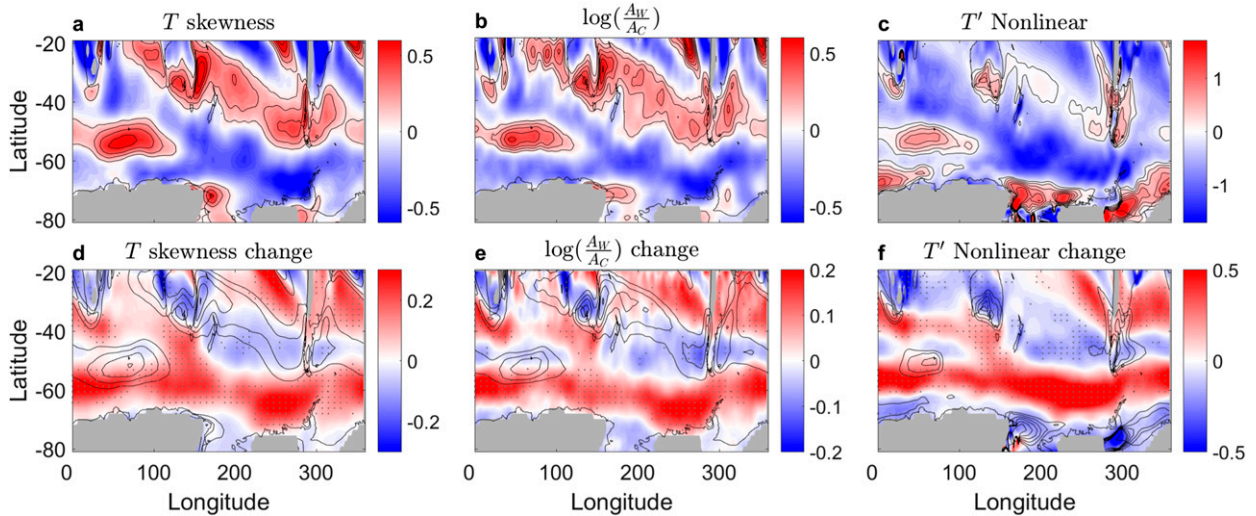


FIG. 10. As in Fig. 3, but for JJA.

the poleward shift of the maximum background temperature gradient and the latter with a decrease in the meridional propagation speeds (and displacements) of warm and cold anomalies. The decrease in meridional displacements is, in turn, consistent with the stronger relative increase of the temperature gradient compared to temperature variance (Fig. S5).

- 4) The temperature tendency composites show the important role of the nonlinear meridional advection in generating the differential advection and thus the skewness. The linear temperature advection term, which only contributes to the perturbation growth and produces a single signed temperature tendency, is averaged out between the passing cyclones and anticyclones. On the contrary, the nonlinear meridional advection term always produces the same temperature tendency dipole and always implies that warm anomalies move poleward and cold anomalies move equatorward, thus leading to differential skewness.
- 5) By construction, the linear approximation used by *STH* [given in Eq.(1)] cannot capture the skewness and its projected changes. Here, we extend the linear approximation and derive an approximate expression for the nonlinear temperature advection [given in Eqs.(7) or (8)] under simplified conditions to include the second-order correction to the temperature anomaly. This expression makes it clear why the skewness is always positive (negative) on the poleward (equatorward) side of the maximum temperature variance, since it involves the meridional gradient of the latter. This expression can also be evaluated in the reanalysis and CMIP5 models and

is shown to capture the general structure of the skewness and its projected changes (Fig. 3).

When the storm track is less zonally symmetric, such as in the SH during JJA (Fig. 10), when the jet is spiraling, the nonlinear approximation given in expression (8) does not approximate well the temperature skewness (cf. Figs. 10a,c). This is probably because stationary waves and zonal gradients not included in our simplified model become important. However, the ratio of the mean intensities from the tracking still recovers remarkably well the skewness structure (Fig. 10b). Hence, the dynamical tracking approach can still be useful for investigating projected temperature variability changes even in more complicated situations such as in the NH, when zonal asymmetries are present. This will be the subject of a future study.

Acknowledgments. This research has been supported by the James S. McDonnell Foundation for complex systems, and by the European Research Council Advanced Grant (ACRCC) ‘‘Understanding the atmospheric circulation response to climate change’’, project 339390. The authors thank Nili Harnik, John Methven, and Marianna Linz for some helpful discussions, and the reviewers for their constructive comments. The data were obtained from the World Data Center for Climate (WDCC). We acknowledge the World Climate Research Programmes’ Working Group on Coupled Modelling, which is responsible for CMIP, and we thank the climate modelling groups for producing and making available their model output. For CMIP, the US Department of Energy Program for Climate Model Diagnosis and Intercomparison provides coordinating support and led development of software infrastructure

in partnership with the Global Organization for Earth System Science Portals. We also thank B. Stevens and M. Esch from the Max-Planck Institute for Meteorology, for providing the high-temporal-resolution data of ECHAM6 (MPI-ESM-LR) necessary for the temperature tendency analysis. The ERA-Interim data used in this study have been obtained from the ECMWF data server: <http://apps.ecmwf.int/datasets/>.

APPENDIX

Derivation of the Nonlinear Approximation

In this appendix, we derive the approximation of the nonlinear temperature advection given in expression (7).

We assume that the background state satisfies $\bar{u} = 0$, $\bar{v} = 0$, $\partial\bar{T}/\partial x = 0$, and $\partial\bar{T}/\partial y = C$ (positive constant, to mimic the SH), and the flow is nondivergent, such that $(\partial u'/\partial x) + (\partial v'/\partial y) = 0$.

We investigate the second-order solution of Eq. (5), given by

$$\frac{\partial T'}{\partial t} = -u' \frac{\partial T'}{\partial x} - v' \frac{\partial T'}{\partial y} = -\frac{\partial(u'T')}{\partial x} - \frac{\partial(v'T')}{\partial y}, \quad (\text{A1})$$

where the latter equality is achieved using the nondivergence of the velocity field.

We use the linear approximation solution to estimate the nonlinear tendency by plugging T' from Eq. (6) and rearranging, which gives

$$\frac{\partial T'}{\partial t} = \frac{\partial\bar{T}}{\partial y} \left[\frac{\partial}{\partial x}(u'\eta) + \frac{\partial}{\partial y}(v'\eta) \right]. \quad (\text{A2})$$

Motivated by the composite analysis, we neglect the first term on the RHS of Eq. (A2), since u' is small at the meridional position where T' or η' are maximum [see Fig. S6, where we show that $\partial/\partial x(u'T')$ is indeed significantly smaller than $\partial/\partial y(v'T')$].

Hence, we find

$$\frac{\partial T'}{\partial t} \approx \frac{\partial\bar{T}}{\partial y} \frac{\partial}{\partial y}(v'\eta) \approx \frac{\partial\bar{T}}{\partial y} \frac{\partial}{\partial y} \left(\frac{1}{2} \frac{\partial\eta^2}{\partial t} \right), \quad (\text{A3})$$

where we have used $\partial\eta/\partial t = v'$. Rearranging the partial derivatives and time integrating then gives

$$T'_{\text{NL}} \approx \frac{1}{2} \frac{\partial\bar{T}}{\partial y} \frac{\partial(\eta^2)}{\partial y}, \quad (\text{A4})$$

which is our approximation to the temperature perturbation due to nonlinear meridional advection, given in Eq. (7).

Summing up the linear and nonlinear contributions, we find

$$T' \approx -\eta \frac{\partial\bar{T}}{\partial y} + \frac{1}{2} \frac{\partial\bar{T}}{\partial y} \frac{\partial(\eta^2)}{\partial y}. \quad (\text{A5})$$

Note that a central aspect of the differential skewness is the localization of T'^2 or η^2 . In our heuristic model, the stirring waves are propagating preferentially around the latitude where \bar{T}'^2 and η^2 maximize and around which skewness is formed.

An alternative way to obtain expression (A5) is to use the linear approximation, but to take into account that the advection leading to the temperature anomaly is acting on an already perturbed state. This can be accounted for by modifying the background state, such that

$$T' \approx -\eta \left(\frac{\partial\bar{T}}{\partial y} + \frac{\partial T'_L}{\partial y} \right). \quad (\text{A6})$$

Inserting the linear approximation $T'_L \approx -\eta \partial\bar{T}/\partial y$ (where $\partial\bar{T}/\partial y$ is y independent) in the second term yields

$$T' \approx -\eta \frac{\partial\bar{T}}{\partial y} + \frac{\partial\bar{T}}{\partial y} \eta \frac{\partial\eta}{\partial y}, \quad (\text{A7})$$

or

$$T' \approx -\eta \frac{\partial\bar{T}}{\partial y} + \frac{1}{2} \frac{\partial\bar{T}}{\partial y} \frac{\partial(\eta^2)}{\partial y}, \quad (\text{A8})$$

which recovers Eq. (A5). This is essentially an iterative procedure to recover the next-order correction to the linear approximation.

REFERENCES

- Arrhenius, S., 1896: On the influence of carbonic acid in the air upon the temperature of the ground. *London Edinburgh Dublin Philos. Mag. J. Sci.*, **41**, 237–276, <https://doi.org/10.1080/14786449608620846>.
- Barnes, E. A., and L. Polvani, 2013: Response of the midlatitude jets, and of their variability, to increased greenhouse gases in the CMIP5 models. *J. Climate*, **26**, 7117–7135, <https://doi.org/10.1175/JCLI-D-12-00536.1>.
- Bindoff, N. L., and Coauthors, 2013: Detection and attribution of climate change: From global to regional. *Climate Change 2013: The Physical Science Basis*, T. F. Stocker et al., Eds., Cambridge University Press, 867–952, https://www.ipcc.ch/site/assets/uploads/2018/02/WG1AR5_Chapter10_FINAL.pdf.
- Bretherton, F. P., 1966: Baroclinic instability and the short wavelength cut-off in terms of potential vorticity. *Quart. J. Roy. Meteor. Soc.*, **92**, 335–345, <https://doi.org/10.1002/qj.49709239303>.
- Cohen, J., and Coauthors, 2014: Recent Arctic amplification and extreme mid-latitude weather. *Nat. Geosci.*, **7**, 627–637, <https://doi.org/10.1038/ngeo2234>.
- Coumou, D., A. Robinson, and S. Rahmstorf, 2013: Global increase in record-breaking monthly-mean temperatures. *Climatic Change*, **118**, 771–782, <https://doi.org/10.1007/s10584-012-0668-1>.

- Dee, D. P., and Coauthors, 2011: The ERA-Interim reanalysis: Configuration and performance of the data assimilation system. *Quart. J. Roy. Meteor. Soc.*, **137**, 553–597, <https://doi.org/10.1002/qj.828>.
- de Vries, H., R. J. Haarsma, and W. Hazeleger, 2012: Western European cold spells in current and future climate. *Geophys. Res. Lett.*, **39**, L04706, <https://doi.org/10.1029/2011GL050665>.
- Donat, M. G., and L. V. Alexander, 2012: The shifting probability distribution of global daytime and night-time temperatures. *Geophys. Res. Lett.*, **39**, L14707, <https://doi.org/10.1029/2012GL052459>.
- Easterling, D. R., G. A. Meehl, C. Parmesan, S. A. Changnon, T. R. Karl, and L. O. Mearns, 2000: Climate extremes: Observations, modeling, and impacts. *Science*, **289**, 2068–2074, <https://doi.org/10.1126/science.289.5487.2068>.
- Emanuel, K., M. Fantini, and A. Thorpe, 1987: Baroclinic instability in an environment of small stability to slantwise moist convection. Part I: Two-dimensional models. *J. Atmos. Sci.*, **44**, 1559–1573, [https://doi.org/10.1175/1520-0469\(1987\)044<1559:BIIAEO>2.0.CO;2](https://doi.org/10.1175/1520-0469(1987)044<1559:BIIAEO>2.0.CO;2).
- Fischer, E. M., and C. Schär, 2009: Future changes in daily summer temperature variability: Driving processes and role for temperature extremes. *Climate Dyn.*, **33**, 917–935, <https://doi.org/10.1007/s00382-008-0473-8>.
- Francis, J. A., and S. J. Vavrus, 2012: Evidence linking Arctic amplification to extreme weather in mid-latitudes. *Geophys. Res. Lett.*, **39**, L06801, <https://doi.org/10.1029/2012GL051000>.
- Gao, Y., L. R. Leung, J. Lu, and G. Masato, 2015: Persistent cold air outbreaks over North America in a warming climate. *Environ. Res. Lett.*, **10**, 044001, <https://doi.org/10.1088/1748-9326/10/4/044001>.
- Garfinkel, C. I., and N. Harnik, 2017: The non-Gaussianity and spatial asymmetry of temperature extremes relative to the storm track: The role of horizontal advection. *J. Climate*, **30**, 445–464, <https://doi.org/10.1175/JCLI-D-15-0806.1>.
- Hansen, J., M. Sato, and R. Ruedy, 2012: Perception of climate change. *Proc. Natl. Acad. Sci. USA*, **109**, E2415–E2423, <https://doi.org/10.1073/pnas.1205276109>.
- Hassanzadeh, P., Z. Kuang, and B. F. Farrell, 2014: Responses of midlatitude blocks and wave amplitude to changes in the meridional temperature gradient in an idealized dry GCM. *Geophys. Res. Lett.*, **41**, 5223–5232, <https://doi.org/10.1002/2014GL060764>.
- Hodges, K. I., 1995: Feature tracking on the unit sphere. *Mon. Wea. Rev.*, **123**, 3458–3465, [https://doi.org/10.1175/1520-0493\(1995\)123<3458:FTOTUS>2.0.CO;2](https://doi.org/10.1175/1520-0493(1995)123<3458:FTOTUS>2.0.CO;2).
- , 1996: Spherical nonparametric estimators applied to the UGAMP model integration for AMIP. *Mon. Wea. Rev.*, **124**, 2914–2932, [https://doi.org/10.1175/1520-0493\(1996\)124<2914:SNEATT>2.0.CO;2](https://doi.org/10.1175/1520-0493(1996)124<2914:SNEATT>2.0.CO;2).
- , 1999: Adaptive constraints for feature tracking. *Mon. Wea. Rev.*, **127**, 1362–1373, [https://doi.org/10.1175/1520-0493\(1999\)127<1362:ACFFT>2.0.CO;2](https://doi.org/10.1175/1520-0493(1999)127<1362:ACFFT>2.0.CO;2).
- Holmes, C. R., T. Woollings, E. Hawkins, and H. de Vries, 2016: Robust future changes in temperature variability under greenhouse gas forcing and the relationship with thermal advection. *J. Climate*, **29**, 2221–2236, <https://doi.org/10.1175/JCLI-D-14-00735.1>.
- Holzer, M., 1996: Asymmetric geopotential height fluctuations from symmetric winds. *J. Atmos. Sci.*, **53**, 1361–1379, [https://doi.org/10.1175/1520-0469\(1996\)053<1361:AGHFFS>2.0.CO;2](https://doi.org/10.1175/1520-0469(1996)053<1361:AGHFFS>2.0.CO;2).
- Hoskins, B., and K. Hodges, 2002: New perspectives on the Northern Hemisphere winter storm tracks. *J. Atmos. Sci.*, **59**, 1041–1061, [https://doi.org/10.1175/1520-0469\(2002\)059<1041:NPNOTH>2.0.CO;2](https://doi.org/10.1175/1520-0469(2002)059<1041:NPNOTH>2.0.CO;2).
- , and —, 2005: A new perspective on the Southern Hemisphere storm tracks. *J. Climate*, **18**, 4108–4129, <https://doi.org/10.1175/JCLI3570.1>.
- Huntingford, C., P. D. Jones, V. N. Livina, T. M. Lenton, and P. M. Cox, 2013: No increase in global temperature variability despite changing regional patterns. *Nature*, **500**, 327–330, <https://doi.org/10.1038/nature12310>.
- Huybers, P., K. A. McKinnon, A. Rhines, and M. Tingley, 2014: U.S. daily temperatures: The meaning of extremes in the context of nonnormality. *J. Climate*, **27**, 7368–7384, <https://doi.org/10.1175/JCLI-D-14-00216.1>.
- Linz, M., G. Chen, and Z. Hu, 2018: Large-scale atmospheric control on non-Gaussian tails of midlatitude temperature distributions. *Geophys. Res. Lett.*, **45**, 9141–9149, <https://doi.org/10.1029/2018GL079324>.
- Loikith, P. C., and A. J. Broccoli, 2012: Characteristics of observed atmospheric circulation patterns associated with temperature extremes over North America. *J. Climate*, **25**, 7266–7281, <https://doi.org/10.1175/JCLI-D-11-00709.1>.
- , and Coauthors, 2015: Surface temperature probability distributions in the NARCCAP hindcast experiment: Evaluation methodology, metrics, and results. *J. Climate*, **28**, 978–997, <https://doi.org/10.1175/JCLI-D-13-00457.1>.
- Luxford, F., and T. Woollings, 2012: A simple kinematic source of skewness in atmospheric flow fields. *J. Atmos. Sci.*, **69**, 578–590, <https://doi.org/10.1175/JAS-D-11-089.1>.
- Manabe, S., and R. T. Wetherald, 1975: The effects of doubling the CO₂ concentration on the climate of a general circulation model. *J. Atmos. Sci.*, **32**, 3–15, [https://doi.org/10.1175/1520-0469\(1975\)032<0003:TEODTC>2.0.CO;2](https://doi.org/10.1175/1520-0469(1975)032<0003:TEODTC>2.0.CO;2).
- , and —, 1980: On the distribution of climate change resulting from an increase in CO₂ content of the atmosphere. *J. Atmos. Sci.*, **37**, 99–118, [https://doi.org/10.1175/1520-0469\(1980\)037<0099:OTDOCC>2.0.CO;2](https://doi.org/10.1175/1520-0469(1980)037<0099:OTDOCC>2.0.CO;2).
- Newman, W. I., B. D. Malamud, and D. L. Turcotte, 2010: Statistical properties of record-breaking temperatures. *Phys. Rev. E*, **82**, 066111, <https://doi.org/10.1103/PhysRevE.82.066111>.
- Perron, M., and P. Sura, 2013: Climatology of non-Gaussian atmospheric statistics. *J. Climate*, **26**, 1063–1083, <https://doi.org/10.1175/JCLI-D-11-00504.1>.
- Petoukhov, V., A. V. Eliseev, R. Klein, and H. Oesterle, 2008: On statistics of the free-troposphere synoptic component: An evaluation of skewnesses and mixed third-order moments contribution to the synoptic-scale dynamics and fluxes of heat and humidity. *Tellus*, **60A**, 11–31, <https://doi.org/10.1111/j.1600-0870.2007.00276.x>.
- Pithan, F., and T. Mauritsen, 2014: Arctic amplification dominated by temperature feedbacks in contemporary climate models. *Nat. Geosci.*, **7**, 181–184, <https://doi.org/10.1038/ngeo2071>.
- Proistosescu, C., A. Rhines, and P. Huybers, 2016: Identification and interpretation of nonnormality in atmospheric time series. *Geophys. Res. Lett.*, **43**, 5425–5434, <https://doi.org/10.1002/2016GL068880>.
- Rhines, A., and P. Huybers, 2013: Frequent summer temperature extremes reflect changes in the mean, not the variance. *Proc. Natl. Acad. Sci. USA*, **110**, E546, <https://doi.org/10.1073/pnas.1218748110>.
- Ruff, T. W., and J. D. Neelin, 2012: Long tails in regional surface temperature probability distributions with implications for extremes under global warming. *Geophys. Res. Lett.*, **39**, L04704, <https://doi.org/10.1029/2011GL050610>.
- Sardeshmukh, P. D., G. P. Compo, and C. Penland, 2015: Need for caution in interpreting extreme weather statistics. *J. Climate*, **28**, 9166–9187, <https://doi.org/10.1175/JCLI-D-15-0020.1>.

- Schär, C., P. L. Vidale, D. Lüthi, C. Frei, C. Häberli, M. A. Liniger, and C. Appenzeller, 2004: The role of increasing temperature variability in European summer heatwaves. *Nature*, **427**, 332–336, <https://doi.org/10.1038/nature02300>.
- Schneider, T., T. Bischoff, and H. Ploetka, 2015: Physics of changes in synoptic midlatitude temperature variability. *J. Climate*, **28**, 2312–2331, <https://doi.org/10.1175/JCLI-D-14-00632.1>.
- Screen, J. A., 2014: Arctic amplification decreases temperature variance in northern mid- to high-latitudes. *Nat. Climate Change*, **4**, 577–582, <https://doi.org/10.1038/nclimate2268>.
- , and I. Simmonds, 2010: The central role of diminishing sea ice in recent Arctic temperature amplification. *Nature*, **464**, 1334–1337, <https://doi.org/10.1038/nature09051>.
- , C. Deser, and L. Sun, 2015: Reduced risk of North American cold extremes due to continued Arctic sea ice loss. *Bull. Amer. Meteor. Soc.*, **96**, 1489–1503, <https://doi.org/10.1175/BAMS-D-14-00185.1>.
- Seneviratne, S. I., D. Lüthi, M. Litschi, and C. Schär, 2006: Land-atmosphere coupling and climate change in Europe. *Nature*, **443**, 205–209, <https://doi.org/10.1038/nature05095>.
- Swanson, K. L., and R. T. Pierrehumbert, 1997: Lower-tropospheric heat transport in the Pacific storm track. *J. Atmos. Sci.*, **54**, 1533–1543, [https://doi.org/10.1175/1520-0469\(1997\)054<1533:LTHTIT>2.0.CO;2](https://doi.org/10.1175/1520-0469(1997)054<1533:LTHTIT>2.0.CO;2).
- Taylor, K., R. Stouffer, and G. Meehl, 2012: An overview of CMIP5 and the experiment design. *Bull. Amer. Meteor. Soc.*, **93**, 485–498, <https://doi.org/10.1175/BAMS-D-11-00094.1>.
- Tingley, M. P., and P. Huybers, 2013: Recent temperature extremes at high northern latitudes unprecedented in the past 600 years. *Nature*, **496**, 201–205, <https://doi.org/10.1038/nature11969>.
- Volodin, E. M., and A. Y. Yurova, 2013: Summer temperature standard deviation, skewness and strong positive temperature anomalies in the present day climate and under global warming conditions. *Climate Dyn.*, **40**, 1387–1398, <https://doi.org/10.1007/s00382-012-1447-4>.
- Yin, J. H., 2005: A consistent poleward shift of the storm tracks in simulations of 21st century climate. *Geophys. Res. Lett.*, **32**, L18701, <https://doi.org/10.1029/2005GL023684>.